

# 3D-Printed Passive Reflectors for mmWave Beam Steering via Binary Aperture Control

Mohammed E. Eltayeb, *Member, IEEE*

arXiv:2601.19087v1 [eess.SY] 27 Jan 2026

**Abstract**—This paper presents a theory-to-hardware framework for fully passive millimeter-wave beam control aimed at extending indoor coverage. The reflecting aperture is modeled using an equivalent array-factor formulation in which each passive element contributes a reradiated field determined by the incident and desired departure angles. Building on this model, we develop two implementation-friendly passive design approaches: (i) *binary (1-bit) spatial masking*, which enables beam steering and multi-beam synthesis by selecting element participation on a dense lattice via an ON/OFF metallization pattern, and (ii) *diffraction-order (periodic) steering*, which exploits controlled aperture periodicity to place selected diffraction orders at prescribed angles. Theoretical analysis characterizes the asymptotic activation behavior of the binary mask and establishes a distribution-free lower-bound on the achievable gain. Prototypes are realized using a copper-backed 3D-printed substrate with stencil-guided conductive ink deposition. 60 GHz over-the-air measurements in single- and multi-beam configurations validate the predicted steering behavior. Theoretical and experimental results demonstrate that fully passive, binary-coded apertures can provide deterministic beam control and offer a scalable alternative to power-consuming reconfigurable surfaces for static indoor links.

**Index Terms**—Millimeter-wave reflectors, fully passive beam-forming, binary aperture control, ON/OFF spatial masking, diffraction-order steering, electromagnetic environment shaping, 3D-printed metasurfaces.

## I. INTRODUCTION

**M**ILLIMETER-WAVE (mmWave, 30–300 GHz) and terahertz (THz, 0.1–10 THz) frequency bands are key enablers of next-generation wireless systems. These bands offer wide contiguous bandwidths for multi-Gbps transmission and enable highly directive apertures for high-angular-resolution spatial selectivity and sensing [1]–[3]. However, the short wavelengths that enable narrow beams also exacerbate propagation impairments such as increased free-space path loss, frequency-dependent atmospheric absorption, and severe penetration losses that make mmWave links highly sensitive to blockages [4], [5]. In practical indoor and dense urban environments, intermittent line-of-sight (LoS) obstruction by moving objects and clutter can induce rapid link degradation or outages. These vulnerabilities motivate *electromagnetic environment shaping* to enable non-line-of-sight (NLoS) coverage extension and deterministic link redirection.

This work was supported by the National Science Foundation under Grant No. NSF-2243089.

Mohammed E. Eltayeb is with the Department of Electrical and Electronic Engineering, California State University, Sacramento, USA. (Email: mohammed.eltayeb@csus.edu)

Reconfigurable intelligent surfaces (RIS) provide one approach to environment shaping. These surfaces employ tunable elements (e.g., varactors, liquid crystals, and MEMS) to dynamically control reflection coefficients and redirect incident wavefronts [3], [6]–[9]. Despite their versatility, practical mmWave RIS implementations incur nonidealities due to quantized phase errors and mutual coupling, and rely on CSI acquisition and active control circuitry that impose non-negligible power and system overhead.

To reduce control and fabrication complexity, recent work investigated 1-bit binary reflector/RIS architectures [10]–[15]. For example, [10] demonstrated a binary-phase tunable mmWave RIS around 28.5 GHz using PIN-diode unit cells (elements), while [11] reported a 60 GHz electronically reconfigurable reflectarray based on single-bit phase shifters for beam steering. More recently, [12] mitigated undesired grating lobes encountered in conventional 1-bit RIS by introducing fixed pseudo-random per-element phase delays (implemented as unit-cell delay-line offsets) prior to binary (0/π) switching. This broke the periodic quantization-error pattern, redistributed the lobe energy into lower sidelobes, and enabled higher-resolution beam steering with a single-bit control network. Related transmission-type 1-bit programmable metasurfaces in the Ka-band has also been demonstrated, including a 1-bit transmission-type digital programmable coding metasurface enabling multifunctional beam shaping [13], and a wideband 1-bit reconfigurable transmission unit cell [14]. More broadly, 1-bit reconfigurable architectures relied on active switches and scalable bias/control networks [15]. While 1-bit approaches reduced phase resolution and control overhead relative to multi-bit RIS, they still depended on carefully engineered unit-cell responses and scalable biasing/routing and control infrastructure whose complexity and overhead scale unfavorably with aperture size.

These challenges motivated renewed interest in *fully passive* reflectors for static or quasi-static deployments (e.g., corridors, factory floors, and indoor mmWave access points), where power-free operation, mechanical robustness, and fabrication simplicity are highly desirable. In such environments, appropriately engineered passive apertures can enhance NLoS coverage by redirecting incident beams toward desired target directions. A wide range of passive mmWave/THz reflectors has therefore been explored in the literature. These range from simple metallic plates and canonical geometries [16]–[20] to geometrically optimized and application-specific reflecting surfaces [21]–[23]. These efforts demonstrate that carefully shaped passive surfaces can expand coverage beyond specular reflection, however, they often couple beam control

to geometry-dependent fabrication choices and element-level electromagnetic modeling. A representative example is *MilliMirror* [21], [22], in which a prescribed reflection-phase profile is encoded through height modulation of metal-backed dielectric cuboids. Such height-coded designs can be effective, but they typically require a custom three-dimensional geometry per beam pattern and tight material/metallization tolerances. This significantly increases design complexity and can limit deployment as thin panels mounted on existing walls or ceilings.

In contrast, this paper investigates deterministic control of the reflected aperture response using an extremely simple, fully passive, binary-coded reflector designed for thin, planar installation. We consider a reflecting aperture composed of many passive reflective elements arranged on a dense candidate lattice. Each passive reflecting element is modeled as an equivalent radiator whose far-field contribution is determined by the incident and reradiated directions as shown in Fig. 1. Building on this abstraction, we propose two fully passive beam-synthesis strategies. The first is a deterministic 1-bit synthesis rule that converts a desired continuous aperture phase profile into a binary ON/OFF metallization mask. The second strategy performs periodic (grating-lobe) engineering by selecting an effective element spacing (or equivalently, a periodic activation pattern on the dense lattice) to enforce coherent addition toward a prescribed departure angle for a given incidence angle.

To realize these designs in hardware, we fabricate low-cost, fully passive prototypes using a copper-backed, thin 3D-printed “inkwell” scaffold and stencil-guided conductive paint deposition. A stencil-defined ON/OFF metallization pattern selects which lattice sites participate in the coherent array-factor summation. The aperture is controlled solely through a surface-applied binary mask and requires no active components, biasing, or per-element tuning. The main contributions of this paper are as follows:

- We develop a deterministic 1-bit beam-synthesis algorithm based on a cosine-threshold binary mask that maps a desired far-field objective (single-beam or multi-beam) to a binary ON/OFF aperture distribution.
- We analytically characterize the asymptotic behavior of the proposed cosine-threshold rule and show that, under mild irrationality conditions on the phase increment, the ON/OFF selection converges to a 50% activation ratio as the aperture size grows. We further derive a lower bound on the maximum main-lobe gain loss relative to ideal continuous phase control.
- We develop a complementary fully passive steering strategy based on diffraction-order (grating-lobe) engineering. Using the incident angle and the desired reflection direction, we derive a design rule for the effective period (inter-element spacing) that places the desired grating-lobe (diffraction) order at the target direction.
- We demonstrate that passive beam control can be achieved without per-element geometry optimization or engineered discrete phase states by encoding the aperture distribution on a fixed dense lattice. Unlike height-modulated reflectors (e.g., *MilliMirror* [21], [22]), which

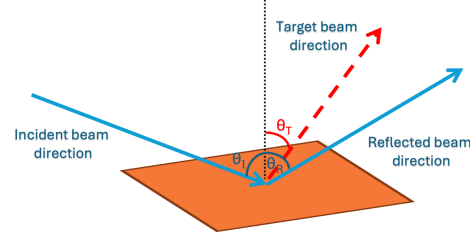


Fig. 1. Equivalent array-factor model for a passive reflecting element. A plane wave impinges at AoA  $\theta_I$  and produces a dominant specular component at  $\theta_R$  (with the sign convention  $\theta_R = -\theta_I$ ). Each passive cell is modeled as an equivalent radiator whose far-field contribution carries the tangential phase associated with the incident and reradiated directions..

encode phase through thickness variation, the proposed approach maintains uniform thickness and simplifies fabrication and planar deployment.

- We fabricate fully passive mmWave reflector prototypes using a copper-backed 3D-printed “inkwell” substrate and stencil-guided conductive paint deposition (metallization). We further validate deterministic single- and multi-beam operation through over-the-air 60 GHz measurements and demonstrate the proposed diffraction-order steering mechanism via uniform period selection.

Together, these contributions establish a low-complexity and fabrication-friendly framework for fully passive reflected-field control to enhance NLoS indoor coverage.

## II. SYSTEM MODEL AND PROBLEM FORMULATION

### A. System Model

We consider a narrowband mmWave downlink in which a transmitting node illuminates a planar, *fully passive* reflecting aperture (reflectarray) that redirects energy toward one or more receivers. For analytical tractability we adopt a one-dimensional (1-D) aperture model where  $M$  electrically small reflecting elements are arranged along the  $x$ -axis with nominal inter-element spacing  $d_0$ . A dominant plane-wave component (beam) impinges on the reflector from an angle of incidence (AoA)  $\theta_I$ , measured from the aperture broadside, and the scattered field is observed in the reflection half-space toward an angle of departure (AoD)  $\theta_T$ . The transmitter and receiver are assumed to employ directive antennas whose boresights are aligned with the reflector normal such that the active aperture is uniformly illuminated.

Under the standard far-field abstraction commonly adopted for RIS, the complex baseband signal observed at a departure angle  $\theta_T$  due to an impinging plane wave from angle  $\theta_I$  can be expressed as [6], [7], [24],

$$p(\theta_T, \theta_I) \triangleq \mathbf{a}^T(\theta_T) \Psi \mathbf{a}(\theta_I), \quad (1)$$

where  $\mathbf{a}(\theta) \in \mathbb{C}^M$  is the array manifold (steering) vector and  $\Psi \in \mathbb{C}^{M \times M}$  is a diagonal matrix that captures the element-wise complex scattering coefficients. The diagonal entry  $[\Psi]_{m,m}$  represents the effective complex reflection coefficient of the  $m$ th element which incorporates both amplitude and phase responses. For a uniform linear lattice, the spatial

coordinates (positions) of the array elements along the the  $x$ -axis are given by

$$x_m \triangleq \left( \frac{M-1}{2} - m \right) d_0, \quad m = 0, 1, \dots, M-1, \quad (2)$$

and the 1-D manifold is

$$\mathbf{a}(\theta) \triangleq [e^{-j k x_0 \sin \theta}, e^{-j k x_1 \sin \theta}, \dots, e^{-j k x_{M-1} \sin \theta}]^T, \quad (3)$$

where  $k = 2\pi/\lambda$  is the free-space wavenumber and  $\lambda$  is the carrier wavelength. Expanding (1) yields the following phasor-summation form

$$p(\theta_T, \theta_I) = \sum_{m=0}^{M-1} [\Psi]_{m,m} e^{-j k x_m (\sin \theta_T + \sin \theta_I)}. \quad (4)$$

Equation (4) shows that the phase progression across the reflective aperture is dependent on the combined phase contributions of the incident and re-radiated plane waves which accumulate with the element distance along the array. In electronically reconfigurable surfaces, the diagonal coefficients in  $\Psi$  can be programmed to enforce coherent combination of the element responses in (4) and maximize gain at a target direction. For passive reflectors with ideal identical elements, the reflection matrix is diagonal with unit entries, i.e.,  $[\Psi]_{m,m} = 1$  for all  $m$ , and the resulting element responses do not, in general, combine coherently in non-specular directions. In this work, we therefore consider purely passive design mechanisms intended to approximate a desired response without bias networks, tunable components, or embedded control electronics.

### B. Problem Formulation

The objective is to design a fully passive reflector that redirects incident energy arriving from AoA  $\theta_I$  toward one or more desired AoDs  $\{\theta_{T,\ell}\}_{\ell=1}^L$  while maintaining a fabrication-friendly structure and avoiding active electronics. Using the scattering response in (4), we seek passive design parameters that shape the angular power pattern  $|p(\theta, \theta_I)|^2$  such that

$$\begin{aligned} \theta \in \{\theta_{T,\ell}\}_{\ell=1}^L \Rightarrow & |p(\theta, \theta_I)|^2 \text{ is maximized,} \\ \theta \notin \{\theta_{T,\ell}\}_{\ell=1}^L \Rightarrow & |p(\theta, \theta_I)|^2 \text{ is minimized (or bounded).} \end{aligned}$$

We pursue this goal using two complementary fully passive mechanisms:

1) *Fixed-aperture beam shaping via 1-bit ON/OFF spatial masking*: We design a binary ON/OFF conductive pattern on a fixed lattice with spacing  $d_0$ , i.e.,

$$[\Psi]_{m,m} = b_m, \quad b_m \in \{0, 1\}, \quad (5)$$

so that beam shaping is achieved by selectively activating or deactivating elements. From (4), the mask  $\{b_m\}$  controls the effective aperture illumination and its spatial spectrum, enabling beam steering, beam splitting, and controlled angular spreading under a strict 1-bit constraint. We synthesize  $\{b_m\}$  by sampling and 1-bit quantization of an ideal continuous profile, and extend to multi-beam operation via superposition followed by quantization.

2) *Diffraction-Order (Grating-Lobe) Steering via Element Spacing Selection*: When sufficient physical aperture is available, beam steering can be achieved using a simple approach based on selecting a uniform inter-element spacing  $\delta$  to control the diffraction orders of the array. Here, a diffraction order refers to a discrete reradiated direction arising from the spatial periodicity of the array. This corresponds to a grating lobe in array terminology. For identical passive elements ( $[\Psi]_{m,m} = 1$ ), the maxima of (4) occur at angles determined by this spacing-induced condition. By appropriately choosing  $\delta$ , a selected diffraction order can be aligned with a target AoD  $\theta_T$ . This yields closed-form steering relationships and enable multi-beam operation when multiple orders are simultaneously supported by the aperture.

### III. PASSIVE BEAM SHAPING VIA FIXED-APERTURE 1-BIT SPATIAL MASK

This section presents a compact, fully passive beam-steering and multi-beam synthesis method based on a fixed-aperture 1-bit spatial mask. Beam formation is realized on a fixed lattice by selecting a subset of reflective elements to contribute to the coherent sum in (4). Each element is either *ON* (metallized and strongly reflecting) or *OFF* (unmetallized and weakly reflecting), inducing a binary aperture weighting that reshapes the angular scattering pattern. Our design strategy is to (i) form the ideal continuous phase profile that would yield perfect addition toward the target AoD(s), and (ii) map that profile to a fabrication-friendly ON/OFF metallization pattern via a cosine-threshold rule introduced in Section III-B.

#### A. Binary Mask Model

Consider a 1-D aperture sampled at  $M$  locations along the  $x$ -axis with nominal spacing  $d_0$  and positions  $x_m$  given in (2). Let  $b_m \in \{0, 1\}$  denote the state of the  $m$ th element, where  $b_m = 1$  corresponds to an *ON* (reflecting) cell and  $b_m = 0$  corresponds to an *OFF* cell. Define the diagonal mask matrix

$$\mathbf{B} \triangleq \text{diag}(b_0, b_1, \dots, b_{M-1}). \quad (6)$$

Under the array-factor abstraction, the complex response toward AoD  $\theta_T$  under incidence from AoA  $\theta_I$  is

$$p(\theta_T, \theta_I) = \mathbf{a}^T(\theta_T) \mathbf{B} \mathbf{a}(\theta_I), \quad (7)$$

which is the specialization of (1) with  $[\Psi]_{m,m} = b_m$ . Expanding (7) yields

$$p(\theta_T, \theta_I) = \sum_{m=0}^{M-1} b_m e^{-j k x_m (\sin \theta_T + \sin \theta_I)}. \quad (8)$$

Equation (8) shows that  $\{b_m\}$  gates the per-element phasors where *ON* elements participate in coherent beam formation while *OFF* elements are suppressed.

*Non-Ideal ON State*: In practice, the ON/OFF abstraction is approximate and the response of an activated element may deviate due to finite conductivity, surface roughness, thickness variations, and fabrication tolerances. These effects can be modeled by

$$\mathbf{B} \rightarrow \text{diag}(\rho_0 b_0, \dots, \rho_{M-1} b_{M-1}), \quad (9)$$

where  $\rho_m \in \mathbb{C}$  denotes the effective complex reflection coefficient of the  $m$ th element. Throughout this paper, we assume ideal binary reflection coefficients with  $\rho_m \equiv 1$  for activated elements ( $b_m = 1$ ) and  $\rho_m \equiv 0$  otherwise, in order to isolate and emphasize the fundamental behavior of the spatial masking mechanism. When  $\rho_m$  is available (e.g., via calibration or electromagnetic modeling), it can be incorporated into the design and analysis.

### B. Closed-Form Mask Construction from an Ideal Phase Profile

We next develop a closed-form 1-bit mask construction for beam synthesis by starting from the ideal continuous-phase reflector profile and then reducing it to a fabrication-friendly binary metallization pattern using a cosine-threshold rule. To improve robustness for finite apertures, we also allow an optional global phase reference (offset) that rotates the threshold boundary prior to binarization.

1) *Ideal Continuous Reflection Phase Profile*: From (8), the  $m$ th element contributes the free-space phase  $-kx_m(\sin \theta_T + \sin \theta_I)$  toward a target AoD  $\theta_T$  under incidence  $\theta_I$ . A fully programmable reflector would apply the compensating phase

$$\phi_m \triangleq kx_m(\sin \theta_T + \sin \theta_I), \quad (10)$$

so that all contributions add in phase at  $\theta_T$ . The sequence  $\{\phi_m\}$  serves as the reference profile for the subsequent 1-bit mapping.

2) *1-Bit Quantization and ON/OFF Mapping*: We first quantize the ideal unit-modulus phasor  $e^{j\phi_m}$  onto the bipolar alphabet  $\{+1, -1\}$  via nearest-neighbor projection on the unit circle as follows

$$\hat{w}_m \triangleq \arg \min_{w \in \{+1, -1\}} |e^{j\phi_m} - w|^2. \quad (11)$$

This projection yields the closed-form rule

$$\hat{w}_m = \text{sgn}(\Re\{e^{j\phi_m}\}) = \text{sgn}(\cos \phi_m) \in \{+1, -1\}. \quad (12)$$

This quantization rule is illustrated in Fig. 2.

Since the fabricated reflector implements a binary *amplitude* response, the bipolar abstraction is mapped to ON/OFF metallization by associating  $+1$  with ON and  $-1$  with OFF as follows

$$b_m \triangleq \frac{\hat{w}_m + 1}{2} \iff b_m = \mathbf{1}\{\cos \phi_m \geq 0\}. \quad (13)$$

This mapping retains elements whose ideal phases lie in the constructive half-plane and suppresses those that would contribute destructively.

3) *Extension to Multiple Target AoDs*: For  $L$  target AoDs  $\{\theta_{T,\ell}\}_{\ell=1}^L$  with complex weights  $\{\alpha_\ell\}_{\ell=1}^L$ , we superpose the ideal ramps and apply the same threshold as follows

$$s_m \triangleq \sum_{\ell=1}^L \alpha_\ell \exp(jk(\sin \theta_{T,\ell} + \sin \theta_I)x_m), \quad (14)$$

$$b_m \triangleq \mathbf{1}\{\Re\{s_m\} \geq 0\}. \quad (15)$$

The resulting binary mask contains dominant spatial-frequency components corresponding to the superposed targets and thereby enables passive multi-beam formation and splitting.

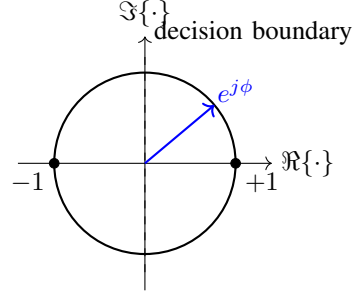


Fig. 2. Geometric view of 1-bit phase quantization on the unit circle. The ideal phasor  $e^{j\phi}$  is mapped to the nearest realizable state  $\{+1, -1\}$  based on the sign of  $\Re\{e^{j\phi}\} = \cos \phi$ . In the proposed hardware, this 1-bit phase-code is then mapped to a physical ON/OFF metallization state.

#### 4) Global Phase Reference for Finite-Aperture Robustness:

For finite apertures, the cosine-threshold operation is sensitive to how the discrete phase samples fall relative to the decision boundary  $\cos(\phi_m) = 0$ . When the inter-element phase increment is (nearly) commensurate with  $\pi$ , a fixed reference can produce highly periodic ON/OFF patterns that partially cancel, leading to pronounced gain drop for finite  $M$ . To mitigate these effects, we introduce a global phase offset  $\psi$ , constant across  $m$ , prior to thresholding

$$b_m(\psi) \triangleq \mathbf{1}\{\cos(\phi_m + \psi) \geq 0\}. \quad (16)$$

The offset  $\psi$  does not alter the AoA/AoD geometry since it does not change the phase-ramp slope and provides a low-complexity means of improving finite-aperture performance. In the following, unless otherwise stated, the implemented ON/OFF mask corresponds to the special case  $\psi = 0$ , and is denoted simply by  $b_m$ .

### C. Thinning Ratio and Efficiency Implications

A direct consequence of ON/OFF masking is aperture thinning. We define the thinning ratio (ON fraction) as

$$\eta_M \triangleq \frac{1}{M} \sum_{m=0}^{M-1} b_m. \quad (17)$$

1) *Asymptotic thinning ratio*: To understand the efficiency implications of binary masking, we examine the asymptotic thinning ratio of the cosine-threshold activation rule as the number of elements grows. This result is formalized in the following lemma.

*Lemma 1 (Asymptotic 50% Thinning Ratio for the Cosine-Threshold Mask):* Consider the cosine-threshold activation rule  $b_m = \mathbf{1}\{\cos(\phi_m) \geq 0\}$ , where the per-element phase progression is  $\phi_{m+1} - \phi_m = kd_0(\sin \theta_T + \sin \theta_I)$ . If the normalized phase increment satisfies

$$\frac{kd_0(\sin \theta_T + \sin \theta_I)}{\pi} \notin \mathbb{Q}, \quad (18)$$

then

$$\lim_{M \rightarrow \infty} \eta_M = \frac{1}{2}. \quad (19)$$

*Proof:* See Appendix A.

Lemma 1 shows that the cosine-threshold construction activates asymptotically half of the available elements, i.e., an approximately 50% aperture fill factor. Condition (18) excludes only degenerate cases in which the element spacing, wavelength, and steering geometry produce a phase increment that is exactly rational relative to the  $\pi$ -periodic sign structure of the cosine threshold. For almost all choices of  $\theta_T$ ,  $\theta_I$ ,  $d_0$ , and  $\lambda$ , the ratio in (18) is irrational; moreover, small perturbations in angle, frequency, or fabrication break exact commensurability. This behavior is illustrated in Fig. 3(a) for  $\theta_I = 60^\circ$  and  $\theta_T = -30^\circ$ . For this configuration, the thinning ratio  $\eta_M$  remains close to 0.5 even for moderate aperture sizes and converges toward 0.5 by  $M \approx 70$ .

#### D. Distribution-free mainlobe gain bound

To quantify gain at the target direction, we compare the achieved reflected response with that of an ideal continuous-phase reflector, which yields a perfectly phase-aligned sum of magnitude  $M$  at  $\theta_T$ . For the ON/OFF mask, the reflected field sum is

$$S_M(\mathbf{b}) \triangleq \sum_{m=0}^{M-1} b_m e^{-j\phi_m}, \quad S_M^* \triangleq \max_{\mathbf{b} \in \{0,1\}^M} |S_M(\mathbf{b})|. \quad (20)$$

Since  $\phi_m$  depends on  $(\theta_I, \theta_T)$ ,  $\{x_m\}$ , and practical phase offsets, the sequence  $\{\phi_m\}$  is geometry- and steering-dependent and its exact statistics may not be known a priori. We therefore adopt a distribution-free (worst-case) analysis. Define the normalized power (mainlobe) gain as

$$\gamma \triangleq \frac{|S_M(\mathbf{b})|^2}{M^2}, \quad \gamma^* \triangleq \max_{\mathbf{b} \in \{0,1\}^M} \gamma = \frac{(S_M^*)^2}{M^2}, \quad (21)$$

where  $\gamma^*$  denotes the maximum achievable normalized gain. A distribution-free lower bound on  $\gamma^*$  is provided in the following lemma.

**Lemma 2 (Distribution-free gain bound for ON/OFF masking):** Consider the sum defined in (20). For arbitrary element locations  $\{x_m\}$  and any incidence and target angles  $(\theta_I, \theta_T)$ , the maximum achievable normalized mainlobe gain satisfies

$$\gamma^* \geq \frac{1}{\pi^2}. \quad (22)$$

*Proof:* See Appendix B.

Fig. 3(b) illustrates the distribution-free performance guarantee established in Lemma 2. Over the range of  $\sin \theta_T + \sin \theta_I$ , the normalized mainlobe gain  $\gamma = |S_M|^2/M^2$  is shown for an ideal continuous-phase reflector, a binary  $\pm 1$  phase mask, and a binary ON/OFF mask. As expected, the  $\pm 1$  phase mask incurs a smaller gain loss than ON/OFF masking because sign reversals can re-phase otherwise destructive contributions, whereas ON/OFF control can only suppress elements, effectively reducing the active aperture. The figure confirms that the lower bound for ON/OFF control is tight in practice. Finally, at  $\sin \theta_T + \sin \theta_I = 0$ , all schemes achieve unit gain ( $\gamma = 1$ ), corresponding to the specular-reflection case AoA = AoD, where coherent reflection is obtained without element deactivation.

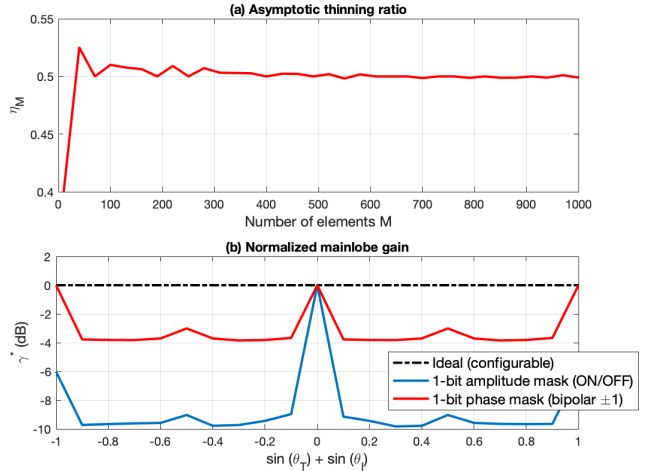


Fig. 3. (a) Thinning ratio  $\eta_M$  versus the number of elements for  $\theta_I = 60^\circ$  and  $\theta_T = -30^\circ$ , illustrating convergence to 0.5 as derived in Lemma 1. (b) Normalized mainlobe gain  $\gamma$  versus  $\sin \theta_T + \sin \theta_I$  for  $M = 64$  and  $d/\lambda = 0.5$  (negative  $\theta_T$  denotes reflection). ON/OFF masking incurs a worst-case loss of 9.94 dB relative to an ideal continuous-phase reflector and  $\approx 6$  dB penalty relative to  $\pm 1$  phase control, consistent with Lemma 2.

#### IV. DIFFRACTION-ORDER (GRATING-LOBE) BEAM STEERING VIA UNIFORM PERIOD SELECTION

Section III introduced fixed-aperture ON/OFF masking as a fabrication-friendly approach to passive steering and beam splitting. Since ON/OFF control can only suppress elements (rather than impose arbitrary phases), it may not guarantee that the strongest beam occurs exactly at the desired  $\theta_T$ . Furthermore, turning elements OFF reduces the number of coherent contributors in (4) and lowers the attainable peak gain relative to an all-ON aperture. We therefore introduce a structured alternative based on uniform-period (diffraction-order) steering. A periodic aperture produces a discrete set of beams indexed by an integer diffraction order. Throughout the paper, diffraction-order steering is used as an umbrella term that includes the classical grating-lobe interpretation.

By selecting the period  $\delta$  (equivalently, using every  $p$ th location of a dense scaffold so  $\delta = pd_0$ ), a chosen diffraction order can be placed at the target direction using closed-form, geometry-driven expressions. While a larger  $\delta$  reduces sampling density for a fixed aperture, the design is specified by only a few parameters (period and order). In the following, we formalize the uniform-period model and derive closed-form relationships between  $(\theta_I, \theta_T)$ , the order index, and the required period  $\delta$ .

##### A. Uniform-Period Array-Factor Model

Consider a linear reflector of  $M$  identical elements with uniform inter-element spacing (period)  $\delta$ . Using the centered indexing of (2), the element coordinates are

$$x_m \triangleq \left( \frac{M-1}{2} - m \right) \delta, \quad m = 0, 1, \dots, M-1. \quad (23)$$

A plane wave impinges from AoA  $\theta_I$  and the scattered field is observed toward AoD  $\theta_T$  in the reflection half-space. The

response is the specialization of (4) with  $[\Psi]_{m,m} = 1$  and spacing  $\delta$  and can be written as

$$p(\theta_T, \theta_I) = \sum_{m=0}^{M-1} e^{-jkx_m(\sin \theta_T + \sin \theta_I)}. \quad (24)$$

Define the tangential wavenumbers  $k_I \triangleq k \sin \theta_I$ , and  $k_T \triangleq k \sin \theta_T$ . Substituting (23) into (24) yields

$$p(\theta_T, \theta_I) = \sum_{m=0}^{M-1} e^{-j(\frac{M-1}{2} - m)\delta(k_I + k_T)}. \quad (25)$$

Equation (25) shows that the per-element phase increment is  $\delta(k_I + k_T)$ . Hence the reflector geometry (via  $\delta$ ) controls the coherent addition across the aperture and can be exploited to steer energy into non-specular directions.

### B. Diffraction Orders and Single-Beam Steering

Because the structure is periodic and uniformly illuminated, (25) admits the closed form [24]

$$p(\theta_T, \theta_I) = e^{-j\frac{(M-1)}{2}\delta(k_I + k_T)} \frac{\sin(\frac{M}{2}\delta(k_I + k_T))}{\sin(\frac{1}{2}\delta(k_I + k_T))}. \quad (26)$$

The principal maxima occur when the inter-element phase progression is an integer multiple of  $2\pi$ , i.e.,

$$\delta(k_I + k_T) = 2\pi n, \quad n \in \mathbb{Z}, \quad (27)$$

or, equivalently,

$$\frac{\delta}{\lambda}(\sin \theta_I + \sin \theta_T) = n. \quad (28)$$

Equation (28) is the diffraction-order condition where each integer  $n$  defines a candidate radiating order whose direction is set by  $(\theta_I, \delta)$ . Solving (28) for the angular location of order  $n$  gives

$$\theta_n = \sin^{-1}\left(n \frac{\lambda}{\delta} - \sin \theta_I\right). \quad (29)$$

1) *Closed-form period for steering to a target AoD*: To align order  $n$  with a desired AoD  $\theta_T$ , enforce  $\theta_n = \theta_T$  in (29), which yields the closed-form period

$$\delta^*(n) = \frac{n\lambda}{\sin \theta_T + \sin \theta_I}. \quad (30)$$

We use the first nonzero order ( $n = \pm 1$ ) for single beam design since it typically yields the smallest period (and therefore the smallest physical span for a fixed  $M$ ). The  $n = 1$  case yeilds

$$\delta^* = \frac{\lambda}{\sin \theta_T + \sin \theta_I}. \quad (31)$$

2) *Interpretation and limits*: Equation (30) provides several useful design insights. Specular reflection corresponds to the zeroth diffraction order ( $n = 0$ ), for which the mirror-like direction  $\theta_T = -\theta_I$  follows directly from (28) and is independent of the period  $\delta$ . In contrast, (30) enables the alignment of a nonzero diffraction order ( $n \neq 0$ ) with a prescribed angle of departure. As  $|\sin \theta_T + \sin \theta_I|$  increases, the corresponding  $\delta^*(n)$  decreases, making engineered non-specular lobes more readily achievable through period selection.

### C. Multi-Beam Operation via Multiple Visible Diffraction Orders

Equation (29) implies that multi-beam behavior is inherent whenever more than one diffraction order radiates into the far field. However, not every integer  $n$  yields a propagating beam. The argument of  $\sin^{-1}(\cdot)$  in (29) must lie in  $[-1, 1]$ , otherwise, the corresponding mode does not carry power to the far field. Therefore, order  $n$  is *visible* only if

$$\left| n \frac{\lambda}{\delta} - \sin \theta_I \right| \leq 1. \quad (32)$$

Solving (32) for the integer range of visible orders yields

$$n_{\min} = \left\lceil \frac{\delta}{\lambda} (\sin \theta_I - 1) \right\rceil, \quad n_{\max} = \left\lfloor \frac{\delta}{\lambda} (\sin \theta_I + 1) \right\rfloor, \quad (33)$$

and hence the number of visible orders (lobes) is

$$N_{\text{orders}} = n_{\max} - n_{\min} + 1. \quad (34)$$

If a secondary target AoD  $\theta_{T,2}$  coincides with one of the visible directions  $\theta_n$  in (29), then the same uniform-period design illuminates that direction without further modification. Otherwise, one may select a different order index  $n$  and redesign  $\delta$  so that another visible order aligns with  $\theta_{T,2}$ , subject to constraints such as physical aperture size, minimum spacing, and maximum number of lobes  $N_{\text{orders}}$ . This provides a simple and fully passive route to multi-beam coverage through diffraction-order engineering.

## V. 3D-PRINTED “INKWELL” PROTOTYPES AND STENCIL-BASED FABRICATION

This section describes a low-cost fabrication method used to realize and experimentally validate the two fully passive beam-engineering mechanisms developed in this paper (i) fixed-aperture 1-bit spatial masking (Section III) and (ii) uniform-period diffraction-order steering (Section IV). Both prototype families implement the physical abstraction in Fig. 1, where each metallized element contributes a phasor to the coherent sum in (4). Beam control is achieved either by (a) gating phasor participation through a binary mask  $b_m$  (i.e.,  $[\Psi]_{m,m} = b_m$ ), or (b) selecting the sampling period  $\delta$  so that a desired diffraction order satisfies (28) (with  $\delta$  determined by (30)). The hardware is strictly passive and relies on a combination of fixed geometry (period selection), binary metallization, and a conductive ground plane.

All prototypes share a common 3D-printed “inkwell” substrate that discretizes a  $90 \times 90$  mm aperture into a dense  $35 \times 35$  candidate grid (1225 wells) with 2.5 mm pitch ( $\lambda/2$  at 60 GHz). Table I summarizes the common computer-aided design (CAD) model, which is exported as a stereolithography (STL) file and used for all prototypes.

### A. Common “Inkwell” Geometry and Relation to the Array Model

Fig. 4(a) shows the bare 3D-printed inkwell base. The aperture is discretized into a uniform candidate lattice with fixed pitch  $d_0 = 2.5$  mm  $\approx \lambda/2$  at 60 GHz. Each candidate

TABLE I

COMMON CAD/STL AND FABRICATION DIMENSIONS FOR THE 3D-PRINTED “INKWELL” REFLECTOR PLATFORM (ALL DESIGNS).

Parameter	Value / Description
Aperture size	$90 \times 90$ mm (square), centered at $(0, 0)$
Candidate grid (scaffold)	$35 \times 35$ wells (1225 locations)
Center-to-center pitch	$d_0 = 2.5$ mm in $x$ and $y$ ( $\approx \lambda/2$ at 60 GHz)
Inkwell opening (front)	$2.2 \times 2.2$ mm square
Inkwell depth	$\approx 0.4$ mm (ink reservoir)
Base thickness	$\approx 0.8$ mm total ( $\sim 0.4$ mm bottom dielectric floor + $\sim 0.4$ mm wall layer)
Stencil thickness	$\approx 0.8$ mm
Stencil aperture	$2.1 \times 2.1$ mm square (slightly smaller than wells)
Substrate material	3D-printed dielectric (PLA/PETG)
Metallization	SilexCore conductive paint [25] deposited into wells (stencil-guided for masks)
Ground plane	Continuous copper tape/sheet on rear face (high reflectivity at 60 GHz)

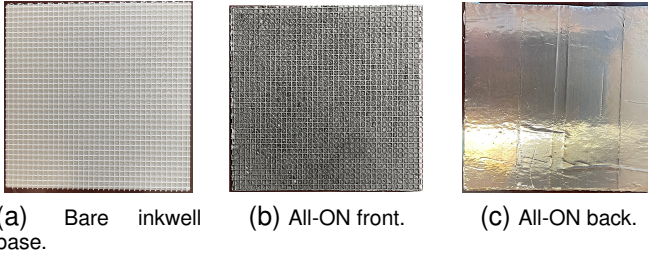


Fig. 4. All-ON reference reflector: (a) bare base, (b) metallized front, (c) copper-backed rear.

location is a square inkwell with a  $2.2 \times 2.2$  mm opening and an approximate depth of 0.4 mm, printed into a dielectric base of total thickness  $\approx 0.8$  mm (a  $\sim 0.4$  mm bottom floor plus a  $\sim 0.4$  mm upper layer forming the well walls). The well walls serve two practical roles: (i) they confine conductive ink during deposition and (ii) they enforce a repeatable metallized footprint across prototypes.

From a modeling perspective, the inkwell grid provides a fixed spatial sampling scaffold for implementing the diagonal interaction matrix  $\Psi$  in (1). For fixed-aperture masking, a subset of wells is metallized to realize  $b_m \in \{0, 1\}$ , thereby modifying the coherent sum in (8). For diffraction-order steering, entire columns are metallized with a uniform inter-column spacing  $\delta$ , realizing the periodic aperture assumed in (28)–(30). Metallization is implemented by filling selected inkwells with a commercial water-based conductive paint [25]. Fig. 4(b) shows the resulting all-ON configuration, in which all wells are metallized. In this context, “ON” refers to a metallized well and the full-grid reflector corresponds to the state where  $b_m = 1$  for all candidate locations. Since this paper targets azimuthal beam shaping, the designed 1-D pattern along the  $x$ -axis is replicated across the  $y$ -axis (constant vertical pitch), producing a striped 2-D aperture that is consistent with a 1-D array-factor interpretation.

### B. Copper-Foil Backing as a Passive Ground Plane

All prototypes use a continuous copper-foil tape layer on the rear side of the printed base to form a conductive ground plane (Fig. 4(c)). This backing is critical at 60 GHz as it provides a high-conductivity termination that increases reflection efficiency and ensures that the front-side pattern modulates a strong reflected field.

### C. Stencil Layer for Repeatable Binary ON/OFF Metallization

For 1-bit masking prototypes, we fabricate a matching 3D-printed stencil that enforces the designed ON/OFF pattern during conductive-ink deposition. The stencil (thickness 0.8 mm) contains square openings of  $2.1 \times 2.1$  mm (slightly smaller than the 2.2 mm inkwell openings) to reduce edge bleeding and improve pattern fidelity. The stencil is closed everywhere except at intended ON locations to map the designed binary sequence  $\{b_m\}$  into a repeatable metallization pattern. Fig. 5 shows representative CAD/STL renderings of the inkwell base and the corresponding stencil for a  $(\theta_I, \theta_T) = (30^\circ, -60^\circ)$  design case. The base defines the fixed  $d_0$  lattice, while the stencil selectively exposes ON wells for conductive-ink deposition.

### D. Prototype Classes, Fabrication Workflow, and Mapping to the Theory

Using the common printing-and-deposition workflow described in this section, we fabricate three prototype classes that correspond directly to the theoretical constructs in Sections III and IV. The prototypes are realized by (i) printing the inkwell base (and a matching stencil), (ii) applying a continuous copper-foil ground plane to the rear face, and (iii) depositing conductive paint into selected inkwells. The stencil restricts deposition to ON wells for all designs.

The full-grid (all-ON) reference reflector is shown in Fig. 4(b), where all  $35 \times 35$  wells are metallized. This prototype realizes a uniform reflective aperture on the fixed  $d_0 = 2.5$  mm scaffold and provides the baseline specular/reference response used to validate the measurement setup.

For fixed-aperture 1-bit spatial masking (Section III), the lattice remains fixed ( $d_0 = 2.5$  mm) and beam control is achieved by metallizing a subset of wells to implement  $b_m \in \{0, 1\}$ . In the model, this corresponds to (8), where the binary sequence gates the per-cell phasors in the coherent sum. In hardware, the same effect is realized via stencil-guided deposition where exposed wells are filled with conductive paint (ON) and covered wells remain unpainted (OFF).

For uniform-period diffraction-order steering (Section IV), beam (lobe) steering is achieved by selecting a uniform inter-column spacing  $\delta$  such that the desired diffraction order satisfies (28) (with  $\delta$  computed from (30)). Practically, we metallize full columns of wells and replicate each active column across all rows.

Fig. 6 shows fabricated 3D-printed passive reflector prototypes for two representative steering configurations,  $(\theta_I, \theta_T) = (30^\circ, -60^\circ)$  and  $(\theta_I, \theta_T) = (45^\circ, -10^\circ)$ . For each angle pair, the figure contrasts a fixed-aperture 1-bit spatial mask with a

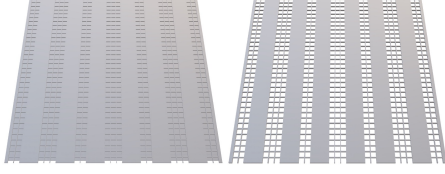


Fig. 5. Inkwell base and matching stencil (CAD/STL).

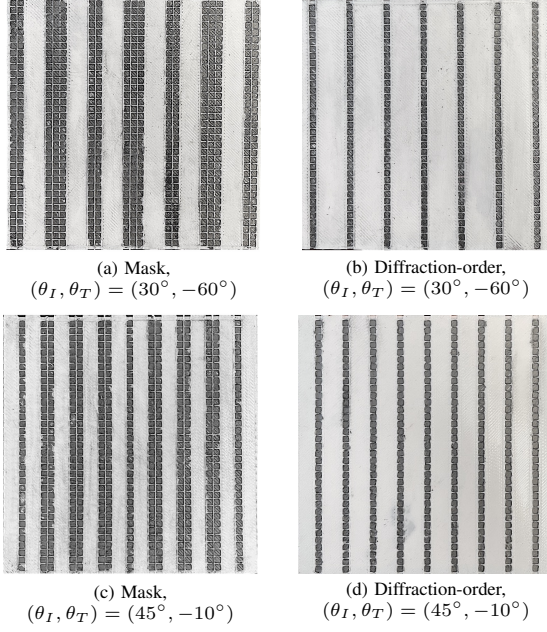


Fig. 6. Fabricated prototypes on the common inkwell substrate (mask vs. diffraction-order).

uniform-period diffraction-order design, both implemented on the same inkwell substrate using a low-complexity, fabrication-friendly process. Although both approaches target the same reflection angles, they differ fundamentally in the mechanism by which the aperture is activated. These prototypes are used in the following section to experimentally validate the proposed beam-control methods through 60 GHz azimuthal measurements.

## VI. RESULTS AND DISCUSSION

This section presents theoretical and experimental results for the proposed fully passive reflector architectures. We first examine the theoretical beam steering and gain characteristics of the binary ON/OFF and diffraction-order designs and compare them against bipolar ( $\pm 1$ ) and ideal configurable reflectors. We then summarize the experimental setup and present 60 GHz over-the-air (OTA) measurements that validate the theoretical results.

### A. Theoretical Results

We begin by analyzing the theoretical performance of the proposed binary ON/OFF beam-synthesis algorithm. For comparison, we also consider an all-ON passive reflector ( $b_m = 1$  for all  $m$ ), a 1-bit bipolar ( $\pm 1$ ) mask, and an ideal configurable

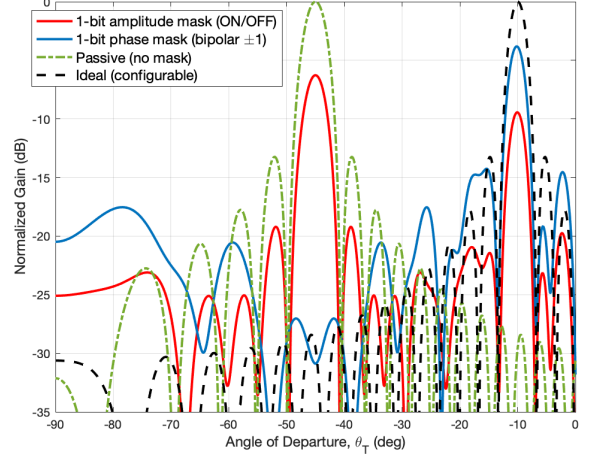


Fig. 7. Theory (60 GHz,  $\theta_I = 45^\circ$ , target  $\theta_T = -10^\circ$ ,  $M = 35$ ,  $d_0/\lambda = 0.5$ ). Normalized mainlobe gain  $\gamma = |S_M|^2/M^2$  for four aperture-control strategies: all-ON, 1-bit ON/OFF (cosine-threshold), 1-bit bipolar ( $\pm 1$ ), and an ideal configurable reflector.

reflector with continuous phase control, which serves as an upper performance bound. Unless otherwise stated, the results assume  $M = 35$  elements, wavelength  $\lambda = 5$  mm, and nominal lattice spacing  $d_0 = 2.5$  mm. All reported curves represent the normalized mainlobe gain  $\gamma = |S_M|^2/M^2 = |p(\theta_T, \theta_I)|^2/M^2$  as defined in Section III-D and Section IV-A.

For  $\theta_I = 45^\circ$  and target angle  $\theta_T = -10^\circ$ , Fig. 7 compares four aperture-control strategies. The all-ON passive aperture produces a dominant specular response at  $\theta_T = -\theta_I = -45^\circ$  and negligible energy in non-specular directions, as expected from uniform weighting. The synthesized 1-bit ON/OFF mask redistributes energy toward the desired direction by selectively activating a subset of the reflector elements. Consistent with Lemma 1, the cosine-threshold construction activates approximately 50% of the elements for generic steering geometries, leading to a reduction in the reflected specular lobe gain. At  $\theta_T = -10^\circ$ , the ON/OFF mask incurs a 9.94 dB loss relative to the ideal configurable reflector, in agreement with the distribution-free bound in Lemma 2. A residual response persists at the specular direction because amplitude-only masking suppresses elements but cannot enforce complete destructive interference. The bipolar ( $\pm 1$ ) mask more closely approximates the ideal configurable response by allowing sign reversals that re-phase otherwise destructive contributions. In this case, the loss relative to the ideal reflector is reduced to approximately 3.94 dB, consistent with the observation that converting the inactive half of the ON/OFF mask into  $-1$  restores coherent contributions and yields an effective 6 dB improvement over amplitude-only gating. In terms of sidelobe behavior, the ON/OFF mask achieves a peak-to-sidelobe ratio (excluding the specular peak) of approximately  $-12.2$  dB, comparable to that of the ideal configurable reflector ( $-13.2$  dB).

When the physical aperture is not constrained, beam steering can alternatively be achieved by selecting a uniform inter-element spacing  $\delta$  to place a grating lobe at the desired angle.

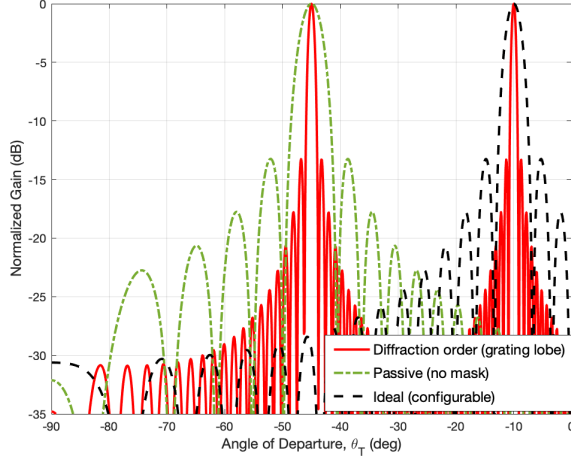


Fig. 8. Theory (60 GHz,  $\theta_I = 45^\circ$ , target  $\theta_T = -10^\circ$ ,  $M = 35$ ). Diffraction-order steering using uniform-period spacing  $\delta = 9.37$  mm with all elements active ( $b_m = 1$ ). The design places a grating lobe at the desired departure angle while the zeroth-order (specular) lobe remains.

For the same  $(\theta_I, \theta_T) = (45^\circ, -10^\circ)$  configuration, Fig. 8 demonstrates this approach using  $\delta = 9.37$  mm with all elements active. The resulting pattern exhibits a strong lobe at the desired direction in addition to the specular component. In this case, the achieved gain is comparable to that of the configurable reflector, with the trade-off that additional visible orders may appear depending on  $\delta$ .

To evaluate multi-beam synthesis via superposition of ideal phase ramps followed by binary thresholding, Fig. 9 presents results for  $\theta_I = 30^\circ$  and target angles  $-60^\circ$  and  $-7.8^\circ$ . The ON/OFF mask redistributes energy toward both intended target directions while retaining a nonzero specular component, consistent with its amplitude-only degrees of freedom. For the ideal configurable reflector, the aperture weights are normalized to split power equally between the two beams, resulting in an expected 3 dB reduction in peak gain per target angle relative to the single-beam case. The bipolar mask closely approximates this ideal configurable response. The ON/OFF mask incurs a larger loss (approximately 6.4 dB relative to the ideal configurable case at the target angles), but nonetheless enables deterministic multi-beam control using a fully passive, fabrication-friendly aperture.

Fig. 10 further illustrates the behavior of uniform-period diffraction-order designs in the same multi-beam configuration. In this case, multiple beams are realized by selecting the inter-element spacing such that the second diffraction order ( $n = 2$ ) is placed within the visible region, thereby producing additional reflected lobes at the desired target angles. As a result, the zeroth (specular) order remains present and higher-order modes may also lie within the visible region, leading to multiple prominent beams. In this configuration, the diffraction-order design achieves higher peak gain at the target angles than the ideal configurable reflector by concentrating energy into narrow grating lobes.

To examine aperture-limited operation, Fig. 11 compares ON/OFF masking, diffraction-order steering, and ideal con-

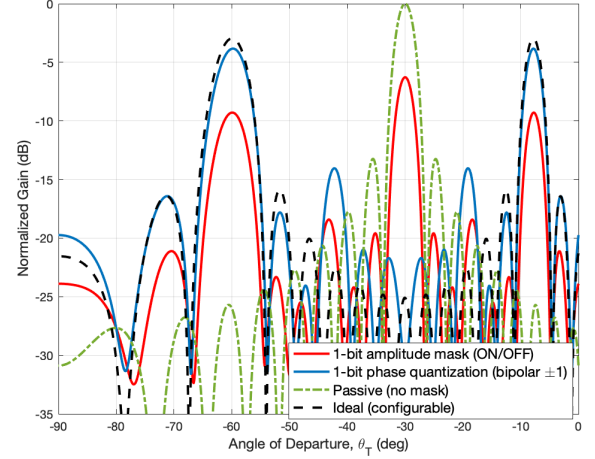


Fig. 9. Theory (60 GHz,  $\theta_I = 30^\circ$ ,  $M = 35$ ): multi-beam synthesis targeting  $\theta_T = -7.8^\circ$  and  $\theta_T = -60^\circ$ . Normalized mainlobe gain  $\gamma$  is shown for the ON/OFF mask, the bipolar ( $\pm 1$ ) mask, and the ideal configurable reflector. The ON/OFF mask redistributes energy toward both targets but incurs an observed loss of  $\approx 6.4$  dB relative to the ideal configurable reflector.

figurable control under fixed physical aperture constraints. In Fig. 11(a), results for  $\theta_I = 45^\circ$  and  $\theta_T = -10^\circ$  are shown. Enforcing a matched aperture requires the diffraction-order design to increase the inter-element spacing to  $\delta = 9.37$  mm, reducing the number of active elements to  $M = 9$ , while the ON/OFF and ideal cases retain  $M = 35$  elements on a dense lattice. Under these constraints, diffraction-order steering suffers a pronounced reduction in normalized gain due to array sparsity, whereas the ON/OFF mask maintains higher performance by exploiting a dense candidate lattice. Fig. 11(b) presents a multi-beam example for  $\theta_I = 60^\circ$  with target angles of  $-30^\circ$  and  $-7.8^\circ$ . Here,  $\delta = 13.66$  mm yields only  $M = 7$  active elements, leading to significant thinning and reduced gain at both target angles. Across both single- and multi-beam cases, these results indicate that ON/OFF masking is preferable in aperture-limited scenarios, while diffraction-order steering becomes attractive primarily when aperture expansion is permissible.

Overall, the theoretical results demonstrate that the proposed ON/OFF masking strategy provides deterministic beam control with predictable loss and sidelobe behavior, offering a favorable trade-off between performance and implementation simplicity. Diffraction-order steering provides a complementary, low-complexity alternative when the aperture size is not a limiting factor.

## B. Experimental Results, Measurement Methodology, and Discussions

### 1) Experimental Setup and Measurement Methodology:

This section describes the 60 GHz over-the-air measurement configuration used to characterize the fabricated passive reflectors and to validate the array-factor formulation developed in Sections III–IV. Measurements are performed for azimuthal AoA/AoD responses with the elevation fixed at  $0^\circ$ , so that the dominant scattering and steering behavior is governed by the

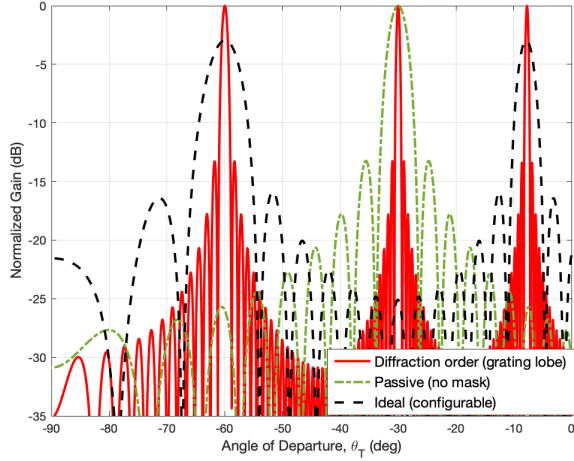


Fig. 10. Theory (60 GHz,  $\theta_I = 30^\circ$ ,  $M = 35$ ): diffraction-order two-beam example with  $\delta = 13.66$  mm. The spacing places grating lobes at the targeted directions and produces higher peak gain at those angles than the ideal configurable case, at the cost of an additional diffraction-order lobe.

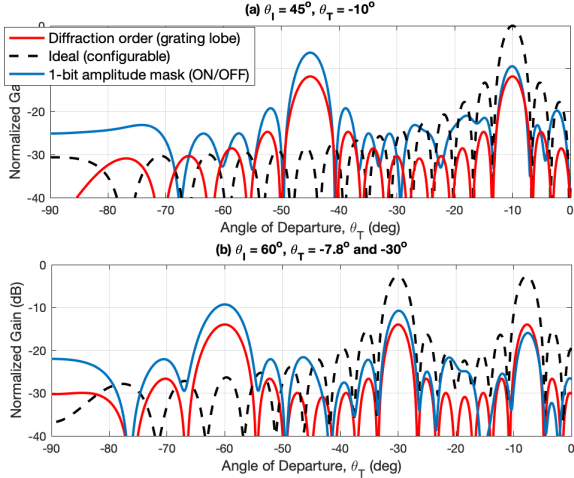


Fig. 11. Theory: aperture-matched comparison of diffraction-order steering and dense ON/OFF masking under fixed physical aperture constraints. (a) Single-beam case for  $\theta_I = 45^\circ$  and target  $\theta_T = -10^\circ$ . (b) Multi-beam case for  $\theta_I = 60^\circ$  with targets at  $\theta_T = -7.8^\circ$  and  $-30^\circ$ . In both cases, diffraction-order steering increases the inter-element spacing  $\delta$ , reducing the number of active elements and resulting in reduced gain.

tangential phase progression along the horizontal  $x$ -axis. All prototypes are measured using identical scan trajectories and RF settings to ensure that differences in the measured patterns arise from the reflector designs rather than the measurement geometry.

Fig. 12 illustrates the measurement setup. Two 60 GHz transceiver evaluation kits (Sivers EVK02001), each equipped with a 16-element phased-array antenna, illuminate and observe the reflector along a constant-radius arc centered on the reflector aperture. For a given configuration, the transmitter is fixed to realize a prescribed azimuth angle of incidence  $\theta_I$  relative to the reflector normal, while the receiver is swept in azimuth in  $5^\circ$  increments to measure the scattered response as a function of departure angle  $\theta_T$  in the reflection half-space.

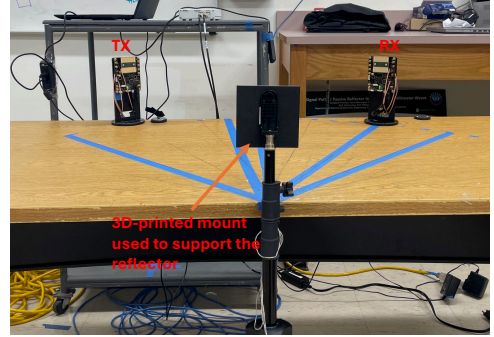


Fig. 12. 60 GHz over-the-air azimuthal sweep measurement setup. The transmitter (TX) is fixed at a prescribed angle of incidence relative to the reflector normal, while the receiver (RX) is swept in azimuth about the reflector to measure the scattered response as a function of departure angle. The reflector is supported by a 3D-printed mount positioned at the center of the measurement arc.

To isolate reflector-induced scattering, two reference measurements are performed: (i) a *mount-only* scan (no reflector) to capture fixture and environmental scattering and the receiver noise floor, and (ii) an *all-ON* reference in which every inkwell on the aperture (here  $35 \times 35$  sites) is metallized and backed by copper, yielding a near-ideal reflective aperture. The received power at azimuth angle  $\theta_T$  is denoted by  $P_{\text{meas}}(\theta_T, \theta_I)$ , with corresponding mount-only and all-ON reference responses denoted by  $P_{\text{mount}}(\theta_T, \theta_I)$  and  $P_{\text{ref}}(\theta_T, \theta_I)$ , respectively.

Measured patterns are processed in the power domain to enable consistent comparison with theoretical results. For each reflector scan, the background-corrected reflected power is computed as

$$\tilde{P}(\theta_T, \theta_I) = \max\{P_{\text{meas}}(\theta_T, \theta_I) - P_{\text{mount}}(\theta_T, \theta_I), 0\},$$

where the  $\max\{\cdot, 0\}$  operator ensures non-negativity after subtraction. The corrected power is then normalized by the maximum value of the same pattern, yielding the normalized measured gain

$$\tilde{g}(\theta_T, \theta_I) = \frac{\tilde{P}(\theta_T, \theta_I)}{\max_{\theta} \tilde{P}(\theta, \theta_I)}. \quad (35)$$

This pattern-wise normalization removes unknown system gains and calibration offsets and enables direct comparison between measured angular gain patterns and theoretical patterns, which are normalized in the same manner over the plotted angular range. All measurements are performed using identical instrument settings (transmit power, array steering, IF bandwidth, averaging, and receiver gain), so the reported results reflect relative pattern shapes rather than absolute link budgets.

2) *Experimental Results*: This subsection compares theoretical patterns with OTA measurements from the fabricated 3D-printed reflector prototypes. All measured patterns were processed using the background subtraction and pattern-wise normalization procedure described in Section VI-B1.

As a first step, Fig. 13 establishes a measurement baseline by comparing the all-ON reflector (Fig. 4(b)) with the mount-only response for an incidence angle  $\theta_I = 45^\circ$ . For this comparison, no background subtraction is applied; instead, the

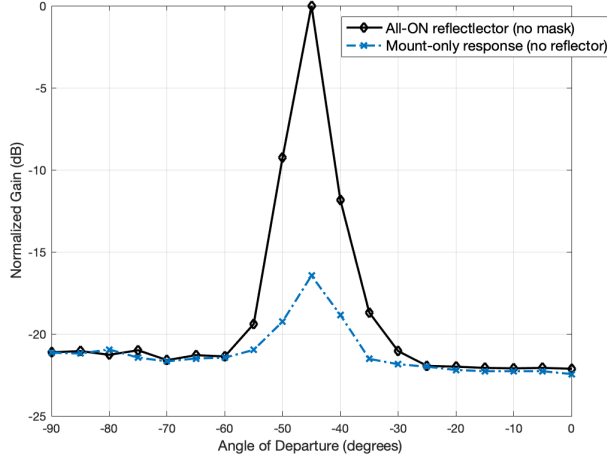


Fig. 13. Experimental: Reference comparison at  $\theta_I = 45^\circ$  showing the normalized azimuthal gain (dB) of the all-ON reflector versus the holder-only (mount) background. The holder-only response remains near the noise floor, confirming reflector-dominated scattering.

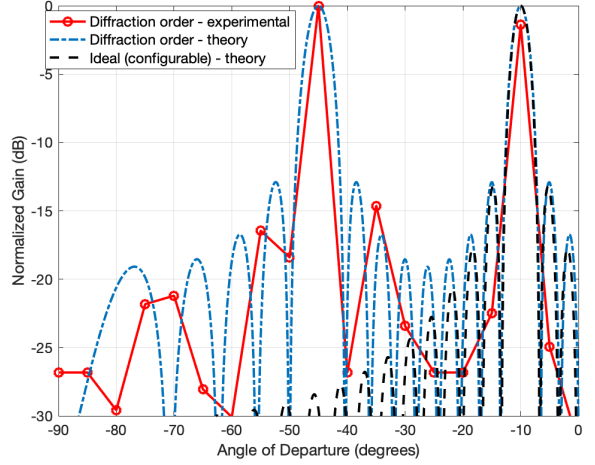


Fig. 15. Experimental: measured and theoretical azimuthal gain patterns for diffraction-order steering with the 3D-printed reflector,  $\theta_I = 45^\circ$  and target  $\theta_T = -10^\circ$ .

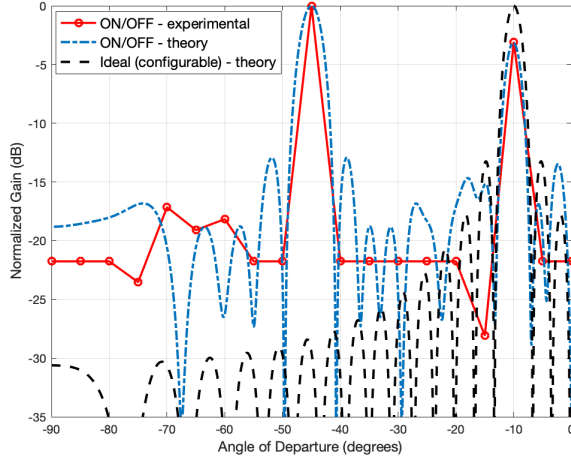


Fig. 14. Experimental: measured and theoretical azimuthal gain patterns for the 3D-printed ON/OFF reflector with  $\theta_I = 45^\circ$  and target  $\theta_T = -10^\circ$ . The measured response closely matches the theoretical response at the intended non-specular target angle.

mount-only response is normalized by the corresponding all-ON reflector response. The all-ON configuration exhibits a strong, well-localized peak at the specular direction  $\theta_T = -\theta_I = -45^\circ$ , while the normalized mount-only response remains near the noise floor across the azimuthal sweep. This behavior confirms that the measured scattering is dominated by the reflector aperture rather than by the mounting structure or surrounding environment, and motivates the use of the mount-only scan as a background reference in subsequent measurements.

To experimentally validate deterministic non-specular beam steering using the fabricated 3D-printed ON/OFF reflector, Fig. 14 compares the measured azimuthal gain of the prototype (Fig. 6(c)) with the corresponding theoretical patterns for  $\theta_I = 45^\circ$  and target angle  $\theta_T = -10^\circ$ . After background

subtraction and normalization, the measured pattern exhibits a clear mainlobe at the intended non-specular direction and closely matches the theoretical beam location and width. Discrepancies in sidelobe levels and deep nulls are attributed to finite aperture size, fabrication tolerances, and residual noise after background subtraction. For reference, the theoretical response of an ideal configurable reflector is also shown and exhibits relatively higher peak gain and deeper sidelobe suppression.

To evaluate diffraction-order (grating-lobe) steering using the fabricated 3D-printed reflector shown in Fig. 6(d), Fig. 15 compares measured azimuthal gain patterns with theoretical patterns for  $\theta_I = 45^\circ$  and target angle  $\theta_T = -10^\circ$ . Measured results are shown alongside the theoretical diffraction-order response derived in Section IV and the theoretical ideal configurable reflector for reference. The measured pattern exhibits pronounced lobes at both the specular direction  $\theta_T = -45^\circ$  and the intended non-specular target direction  $\theta_T = -10^\circ$ , in close agreement with theory. At the target angle, the measured peak gain is approximately 1 dB lower than the theoretical diffraction-order prediction, which can be attributed to conductor losses and residual measurement uncertainty. Despite this small degradation, the measured and theoretical beam locations and relative lobe amplitudes are well aligned.

Next, we evaluate multi-beam synthesis using the binary ON/OFF algorithm applied to the fabricated reflector shown in Fig. 6(a). Fig. 16 compares the measured azimuthal gain pattern with the corresponding theoretical ON/OFF and ideal configurable responses for an incidence angle of  $\theta_I = 30^\circ$  and target angles at  $-7.8^\circ$  and  $-60^\circ$ . The measured pattern reproduces the two intended non-specular beams, with peak locations and beamwidths in close agreement with theory. This confirms that the proposed ON/OFF approach supports deterministic multi-beam operation. A residual response is also observed near the specular direction, consistent with the amplitude-only nature of the ON/OFF mask.

Finally, we evaluate multi-beam synthesis using the

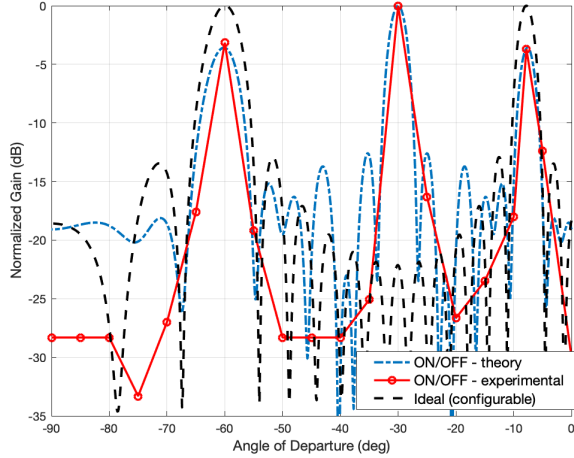


Fig. 16. Experimental: measured and theoretical azimuthal gain patterns for the binary ON/OFF reflector with  $\theta_I = 30^\circ$  and target angles  $\theta_T = -7.8^\circ$  and  $-60^\circ$ .

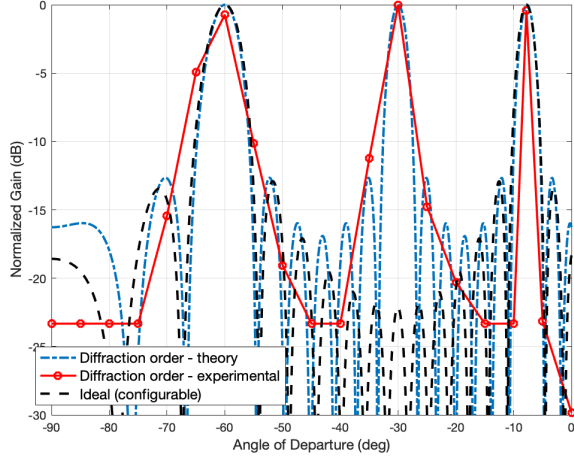


Fig. 17. Experimental: measured and theoretical azimuthal gain patterns for diffraction-order (grating-lobe) steering with  $\theta_I = 30^\circ$  and target angles  $\theta_T = -7.8^\circ$  and  $-60^\circ$ .

diffraction-order method on the fabricated 3D-printed reflector shown in Fig. 6(b). Fig. 17 compares the measured azimuthal gain pattern with the theoretical diffraction-order response and the ideal configurable reflector for an incidence angle  $\theta_I = 30^\circ$  and target angles  $\theta_T = -60^\circ$  and  $-7.8^\circ$ . The measured pattern exhibits pronounced lobes at both target directions, with peak locations and beamwidths closely matching the theoretical diffraction-order response. In addition to the two target beams, a strong lobe is also observed near the specular direction  $\theta_T = -\theta_I = -30^\circ$ , consistent with the presence of the zeroth diffraction order in uniform-period apertures.

Overall, both approaches closely follow the underlying theoretical models and capture key beamforming behaviors typically associated with more complex passive or electronically reconfigurable surfaces, while remaining fully passive, zero power, and rapidly manufacturable using standard laboratory 3D-printing and stencil-based metallization techniques.

## VII. CONCLUSION

This paper presented a theory-to-hardware framework for fully passive millimeter-wave beam engineering using fabrication-friendly 3D-printed reflectors. Two complementary passive mechanisms were developed and validated. The first employs fixed-aperture 1-bit spatial masking, where a binary ON/OFF metallization pattern on a dense  $\lambda/2$  lattice enables compact beam steering and multi-beam synthesis without bias networks or active components. The second exploits diffraction-order (grating-lobe) steering as a geometry-only design strategy, in which selection of a uniform inter-element period aligns a nonzero diffraction order with a desired departure angle while explicitly accounting for the specular and higher-order beams.

Both approaches were realized using a copper-backed 3D-printed “inkwell” aperture with stencil-assisted conductive paint deposition and validated through 60 GHz over-the-air measurements. The results confirm that fully passive, binary, and manufacturable apertures can provide predictable beam control for static indoor NLoS coverage. Although 1-bit amplitude masking incurs a quantifiable efficiency loss relative to electronically reconfigurable surfaces, it offers a practical, zero-power alternative that bridges the gap between simple metallic reflectors and power-consuming reconfigurable architectures.

Future work will address higher-fidelity element and loss modeling, extension to full two-dimensional aperture synthesis for joint azimuth–elevation and polarization control, and the development of semi-static adaptation mechanisms suitable for indoor millimeter-wave environment shaping.

## APPENDIX A PROOF OF LEMMA 1: ASYMPTOTIC 50% ACTIVATION RATIO OF THE COSINE-THRESHOLD MASK

Recall that the element locations are  $x_m = \left(m - \frac{M-1}{2}\right)d_0$ , and define the phase associated with the  $m$ th element as

$$\phi_m \triangleq kx_m(\sin \theta_T + \sin \theta_I), \quad k = \frac{2\pi}{\lambda}.$$

Substituting  $x_m$  into  $\phi_m$  yields the affine phase progression

$$\begin{aligned} \phi_m &= k\left(m - \frac{M-1}{2}\right)d_0(\sin \theta_T + \sin \theta_I) \\ &= \Delta m + \beta_M, \end{aligned} \quad (36)$$

where

$$\Delta \triangleq kd_0(\sin \theta_T + \sin \theta_I), \quad \beta_M \triangleq -\Delta \frac{M-1}{2}.$$

Hence, the phase increment is constant and satisfies  $\phi_{m+1} - \phi_m = \Delta$ . The cosine-threshold activation rule is given by

$$b_m = \mathbf{1}\{\cos(\phi_m) \geq 0\}.$$

Since  $\cos(\cdot)$  is  $2\pi$ -periodic, the activation depends only on  $\phi_m \bmod 2\pi$ . Introduce the normalized phase variable

$$u_m \triangleq \frac{\phi_m}{2\pi} \bmod 1 = \left(\frac{\Delta}{2\pi}m + \frac{\beta_M}{2\pi}\right) \bmod 1.$$

Under the condition  $\Delta/(2\pi) \notin \mathbb{Q}$  (equivalently  $\Delta/\pi \notin \mathbb{Q}$ ), the sequence  $\{u_m\}_{m \geq 0}$  is uniformly distributed on  $[0, 1)$  by

Weyl's equidistribution theorem. Equivalently,  $\phi_m \bmod 2\pi$  is uniformly distributed on the unit circle, with  $u_m$  providing a convenient normalized representation. To relate equidistribution to the cosine-threshold activation rule, define the function

$$f(u) \triangleq \mathbf{1}\{\cos(2\pi u) \geq 0\}.$$

This choice of  $f$  directly encodes the ON/OFF masking rule in normalized phase coordinates, since

$$b_m = \mathbf{1}\{\cos(\phi_m) \geq 0\} = \mathbf{1}\{\cos(2\pi u_m) \geq 0\} = f(u_m).$$

By the defining consequence of equidistribution, for any Riemann-integrable function  $f : [0, 1] \rightarrow \mathbb{R}$ ,

$$\frac{1}{M} \sum_{m=0}^{M-1} f(u_m) \xrightarrow{M \rightarrow \infty} \int_0^1 f(u) du.$$

Applying this result to the above choice of  $f(u)$  yields

$$\begin{aligned} \eta_M &= \frac{1}{M} \sum_{m=0}^{M-1} \mathbf{1}\{\cos(\phi_m) \geq 0\} \\ &= \frac{1}{M} \sum_{m=0}^{M-1} f(u_m) \xrightarrow{M \rightarrow \infty} \int_0^1 \mathbf{1}\{\cos(2\pi u) \geq 0\} du. \end{aligned} \quad (37)$$

The limiting integral corresponds to the fraction of the unit interval for which the cosine-threshold condition is satisfied. Define the set

$$\mathcal{S}_+ \triangleq \{u \in [0, 1] : \cos(2\pi u) \geq 0\} = \left[0, \frac{1}{4}\right] \cup \left[\frac{3}{4}, 1\right).$$

Since the integral of an indicator function equals the Lebesgue measure of its support, we obtain

$$\int_0^1 \mathbf{1}\{\cos(2\pi u) \geq 0\} du = |\mathcal{S}_+| = \frac{1}{2}.$$

Therefore,

$$\eta_M \xrightarrow{M \rightarrow \infty} \frac{1}{2}.$$

This establishes the asymptotic 50% activation ratio and completes the proof of Lemma 1.

## APPENDIX B PROOF OF LEMMA 2

Let

$$S_M(\mathbf{b}) = \sum_{m=0}^{M-1} b_m e^{-j\phi_m}, \quad b_m \in \{0, 1\},$$

and define  $S_M^* \triangleq \max_{\mathbf{b} \in \{0, 1\}^M} |S_M(\mathbf{b})|$ . Recall for a complex number  $z$ , the magnitude can be written as

$$|z| = \max_{\varphi \in [0, 2\pi)} \Re\{e^{-j\varphi} z\}. \quad (38)$$

Applying (38) to  $S_M^*$  and exchanging the two maximizations gives

$$\begin{aligned} S_M^* &= \max_{\mathbf{b} \in \{0, 1\}^M} \max_{\varphi \in [0, 2\pi)} \Re\left\{e^{-j\varphi} \sum_{m=0}^{M-1} b_m e^{-j\phi_m}\right\} \\ &= \max_{\varphi \in [0, 2\pi)} \max_{\mathbf{b} \in \{0, 1\}^M} \sum_{m=0}^{M-1} b_m \cos(\phi_m + \varphi). \end{aligned} \quad (39)$$

For fixed  $\varphi$ , the inner maximization is separable in  $m$  and, since  $b_m \in \{0, 1\}$ , we have

$$\max_{b_m \in \{0, 1\}} b_m \cos(\phi_m + \varphi) = [\cos(\phi_m + \varphi)]_+,$$

where  $[x]_+ \triangleq \max\{x, 0\}$ . Define the normalized objective

$$F_M(\varphi) \triangleq \frac{1}{M} \sum_{m=0}^{M-1} [\cos(\phi_m + \varphi)]_+,$$

so that (39) can be written compactly as

$$\frac{S_M^*}{M} = \max_{\varphi \in [0, 2\pi)} F_M(\varphi). \quad (40)$$

A distribution-free lower bound can be obtained by noting that the maximum of a function is no smaller than its average, hence

$$\max_{\varphi} F_M(\varphi) \geq \frac{1}{2\pi} \int_0^{2\pi} F_M(\varphi) d\varphi. \quad (41)$$

Interchanging the finite sum and the integral (by linearity) and then applying the change of variables  $u = \phi_m + \varphi$  gives

$$\begin{aligned} \frac{1}{2\pi} \int_0^{2\pi} F_M(\varphi) d\varphi &= \frac{1}{M} \sum_{m=0}^{M-1} \frac{1}{2\pi} \int_0^{2\pi} [\cos(\phi_m + \varphi)]_+ d\varphi \\ &= \frac{1}{M} \sum_{m=0}^{M-1} \frac{1}{2\pi} \int_{\phi_m}^{\phi_m + 2\pi} [\cos u]_+ du \\ &= \frac{1}{2\pi} \int_0^{2\pi} [\cos u]_+ du, \end{aligned} \quad (42)$$

where the first equality follows from linearity (the sum is finite and the integrand is bounded), and the second equality follows from  $u = \phi_m + \varphi$  (and  $du = d\varphi$ ). As  $\varphi$  runs over  $[0, 2\pi]$ ,  $u$  runs over the interval  $[\phi_m, \phi_m + 2\pi]$ . Finally, because  $[\cos(\cdot)]_+$  is  $2\pi$ -periodic, the integral over  $[\phi_m, \phi_m + 2\pi]$  equals the integral over  $[0, 2\pi]$ , making each summand independent of  $m$ . Physically, averaging over the global phase-shift  $\varphi$  removes the element-dependent phase offsets and yields a geometry-independent per-element contribution; this is the key step that produces a distribution-free bound.

Note the integrand  $[\cos u]_+$  equals  $\cos u$  on  $u \in [-\frac{\pi}{2}, \frac{\pi}{2}]$  (mod  $2\pi$ ) and is zero elsewhere; therefore

$$\int_0^{2\pi} [\cos u]_+ du = \int_{-\pi/2}^{\pi/2} \cos u du = 2.$$

Combining with (42) yields

$$\frac{1}{2\pi} \int_0^{2\pi} F_M(\varphi) d\varphi = \frac{1}{\pi}.$$

Using (40) and (41) we conclude

$$\frac{S_M^*}{M} = \max_{\varphi} F_M(\varphi) \geq \frac{1}{\pi},$$

which proves the amplitude bound (22). Squaring both sides yields  $\gamma^* \geq 1/\pi^2$ , completing the proof.

## REFERENCES

- [1] C.-X. Wang *et al.*, “On the road to 6G: Visions, requirements, key technologies and testbeds,” *IEEE Commun. Surveys Tuts.*, vol. 25, no. 2, pp. 905–974, Feb. 2023.
- [2] Q. Xue *et al.*, “A survey of beam management for mmWave and THz communications towards 6G,” *IEEE Commun. Surveys Tuts.*, vol. 26, no. 3, pp. 1520–1559, 3rd Quart. 2024.
- [3] M. Ahmed *et al.*, “A survey on RIS advances in terahertz communications: Emerging paradigms and research frontiers,” *IEEE Access*, vol. 12, pp. 173867–173901, 2024.
- [4] Y. Xing and T. S. Rappaport, “Millimeter wave and sub-terahertz spatial statistical channel modeling for wireless communications,” *IEEE J. Sel. Areas Commun.*, vol. 39, no. 6, pp. 1506–1524, Jun. 2021.
- [5] R. W. Heath *et al.*, “An overview of signal processing techniques for millimeter wave MIMO systems,” *IEEE J. Sel. Topics Signal Process.*, vol. 10, no. 3, pp. 436–453, Apr. 2016.
- [6] A. Taha, M. Alrabeiah, and A. Alkhateeb, “Enabling large intelligent surfaces with compressive sensing and deep learning,” *IEEE Access*, vol. 9, pp. 44304–44321, 2021.
- [7] C. Huang, A. Zappone, G. C. Alexandropoulos, M. Debbah, and C. Yuen, “Reconfigurable intelligent surfaces for energy efficiency in wireless communication,” *IEEE Trans. Wireless Commun.*, vol. 18, no. 8, pp. 4157–4170, Aug. 2019.
- [8] M. A. ElMossallamy *et al.*, “Reconfigurable intelligent surfaces for wireless communications: Principles, challenges, and opportunities,” *IEEE Trans. Cogn. Commun. Netw.*, vol. 6, no. 3, pp. 990–1012, Sep. 2020.
- [9] S. V. Hum and J. Perruisseau-Carrier, “Reconfigurable reflectarrays and array lenses for dynamic antenna beam control: A review,” *IEEE Trans. Antennas Propag.*, vol. 62, no. 1, pp. 183–198, Jan. 2014.
- [10] J.-B. Gros, V. Popov, M. A. Odit, V. Lenets, and G. Lerosey, “A reconfigurable intelligent surface at mmWave based on a binary phase tunable metasurface,” *IEEE Open J. Commun. Soc.*, vol. 2, pp. 1055–1064, 2021.
- [11] H. Kamoda, T. Iwasaki, J. Tsumochi, T. Kuki, and O. Hashimoto, “60-GHz electronically reconfigurable large reflectarray using single-bit phase shifters,” *IEEE Trans. Antennas Propag.*, vol. 59, no. 7, pp. 2524–2531, Jul. 2011.
- [12] A. S. Shekhawat, B. G. Kashyap, R. W. Raldiris Torres, F. Shan, and G. C. Trichopoulos, “A millimeter-wave single-bit reconfigurable intelligent surface with high-resolution beam-steering and suppressed quantization lobe,” *IEEE Open J. Antennas Propag.*, vol. 6, no. 1, pp. 311–325, Feb. 2025.
- [13] A. H. Naqvi, D. A. Pham, S. I. H. Shah, and S. Lim, “1-bit transmission-type digital programmable coding metasurface with multi-functional beam-shaping capability for Ka-band applications,” *Micromachines*, vol. 14, no. 6, Art. no. 1250, Jun. 2023.
- [14] T. Huang, W. Fu, D. Lu, Y. Pan, M. Wang, and Y. Yan, “Wideband 1-bit reconfigurable transmission metasurface unit cell design in Ka-band with polarization hold and conversion,” *Scientific Reports*, vol. 13, Art. no. 20076, Nov. 2023.
- [15] P. Li, T. Yang, J. Ren, and Y. Yin, “Design of 1-bit reconfigurable reflectarray based on miniaturized reconfigurable unit,” in *Proc. IEEE Int. Microwave Workshop Series on Antennas and Propagation (IMWS-AMP)*, Chongqing, China, Nov. 2021, pp. 370–372.
- [16] W. Khawaja, O. Ozdemir, Y. Yapici, F. Erden, and I. Guvenc, “Coverage enhancement for NLoS mmWave links using passive reflectors,” *IEEE Open J. Commun. Soc.*, vol. 1, pp. 263–281, 2020.
- [17] O. Ibrahim, R. S. S. Bandari, and M. E. Eltayeb, “LiDAR-aided millimeter-wave range extension using a passive mirror reflector,” in *Proc. IEEE 22nd Consum. Commun. Netw. Conf. (CCNC)*, Jan. 2025, pp. 1–4.
- [18] Z. Peng *et al.*, “An effective coverage scheme with passive-reflectors for urban millimeter-wave communication,” *IEEE Antennas Wireless Propag. Lett.*, vol. 15, pp. 398–401, 2016.
- [19] J. Marroquin, N. Inzali, M. D. Lantz, C. Freeman, A. Ashtekar, A. U. Mulik, and M. E. Eltayeb, “Vision-based autonomous mm-wave reflector using ArUco-driven angle-of-arrival estimation,” in *Proc. IEEE Consum. Commun. Netw. Conf. (CCNC)*, Jan. 2026, pp. 1–6.
- [20] A. P. Ganesh, W. Khawaja, O. Ozdemir, I. Guvenc, H. Nomoto, and Y. Ide, “Propagation measurements and coverage analysis for mmWave and sub-THz frequency bands with transparent reflectors,” in *Proc. IEEE 97th Veh. Technol. Conf. (VTC2023-Spring)*, Jun. 2023, pp. 1–6.
- [21] K. Qian *et al.*, “MilliMirror: 3D printed reflecting surface for millimeter-wave coverage expansion,” in *Proc. 28th Annu. Int. Conf. Mobile Comput. Netw. (MobiCom)*, Oct. 2022, pp. 15–28.
- [22] K. Qian and X. Zhang, “Demo: Fully passive 3D printed reflecting surface for millimeter-wave coverage expansion,” in *Proc. 20th Annu. Int. Conf. Mobile Syst., Appl. Serv. (MobiSys)*, Jun. 2022, pp. 1–2.
- [23] S. Häger, M. Danger, K. Heimann, Y. Gümus, S. Böcker, and C. Wietfeld, “Custom design and experimental evaluation of passive reflectors for mmWave private networks,” in *Proc. IEEE 30th Int. Symp. Local and Metropolitan Area Netw. (LANMAN)*, Boston, MA, USA, 2024, pp. 52–57.
- [24] H. L. Van Trees, *Optimum Array Processing (Detection, Estimation, and Modulation Theory, Part IV)*. Wiley-Interscience, 1st ed., Mar. 2002.
- [25] SilexCore Conductive Paint, Amazon product page. [Online]. Available: <https://www.amazon.com/dp/B0DJTYJD7V>